Magnetic Properties of C80 Endofullerenes

Westerström, Rasmus; Greber, Thomas

Published in:
Endohedral Fullerenes: Electron Transfer and Spin

DOI:
10.1007/978-3-319-47049-8

2017

Document Version:
Publisher's PDF, also known as Version of record

Chapter 11
Magnetic Properties of C_{80} Endofullerenes

Rasmus Westerström and Thomas Greber

Abstract This chapter summarizes the investigations of the endohedral metallofullerenes (EMFs) with a C_{80} carbon shell in view of their magnetic properties, where the recently discovered single-molecule magnetism in dysprosium based species are highlighted.

11.1 Paramagnets

C_{80} is not an abundant species in the fullerene synthesis with the Krätschmer–Huffman method [1]. This can be rationalized with the electronic structure of C_{80} cages, where the highest molecular orbital (HOMO) is not full. However, as it was shown theoretically, C_{80}^{6-} molecules have a large HOMO-LUMO gap and thus predicted to be stable [2]. Some years later the discovery of $Sc_3N@C_{80}$ [3] realized this prediction, since the Sc_3N endohedral unit transfers six electrons to the C_{80} cage. Importantly, it was realized that scandium may be substituted with other trivalent rare earth ions. The 14 rare earth (R) (including promethium) that are trivalent in the Krätschmer–Huffman plasma result in 560 possible endohedral trimetal nitride clusters, where the majority (540) are paramagnetic. Of course, this number increases significantly if additional endohedral compositions are considered, such as the very recently discovered magnetic carbide clusters [4, 5]. We deal here with 4f electron paramagnetism inside a diamagnetic C_{80} cluster. The 4f shell is localized deep inside the corresponding atom and, depending on the filling it can carry large angular momentum and spin that results in magnetic moments of up to 10 μ_B. Importantly, the corresponding anisotropy or deviation from spherical symmetry of the charge distribution indicates the lifting of the Hund ground state

T. Greber (✉)
Physik-Institut, University of Zürich, Zürich, Switzerland
e-mail: greber@physik.uzh.ch

R. Westerström
Synchrotron Radiation Research, Department of Physics,
Lund University, 188 221 00, Lund, Sweden

A.A. Popov (ed.), *Endohedral Fullerenes: Electron Transfer and Spin*,
Nanostructure Science and Technology, DOI 10.1007/978-3-319-47049-8_11

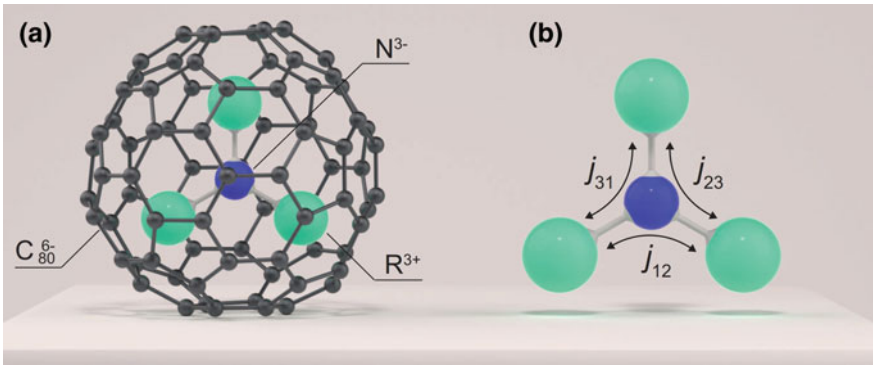

Fig. 11.1 **a** Ball-and stick-model of $R_3N@C_{80}$; R = Rare earth. **b** Model of the endohedral $R_3^{3+}N^{3-}$ unit and the corresponding couplings $j_{i,k}$ that are partly mediated across the N^{3-} ion. From Ref. [19]

degeneracy, a prerequisite for single-molecule magnets [6]. Figure 11.1a displays a model of the $R_3N@C_{80}$ molecule, where the most abundant isomer with icosahedral I_h symmetry is shown. In Fig. 11.1b, the endohedral unit with the possible magnetic interactions that are mediated by the central N^{3-} ion and the magnetic dipole field the two neighbours are shown. The magnetization is ruled by dipolar and exchange interaction between the different constituents. The dipolar interaction is rather strong: Given a distance of 0.35 nm between two magnetic moments of 10 μ_B we get a maximum dipole–dipole interaction of 0.25 meV corresponding to an effective temperature of 3 K. Furthermore, the central N^{3-} ion imposes a ligand field that lifts the Hund ground state degeneracy, orients the anisotropic 4f shell and enables magnetic order.

The gadolinium ($4f^7$) and diamagnetic atoms containing molecules $Gd_nD_{3-n}N@C_{80}$ $n \in \{1, 2, 3\}$, D being diamagnetic D$\in$ {Sc,Y,La,Lu} are closest to an ideal paramagnet, where the magnetic moments follow an external field. This is due to the isotropic 4f charge distribution in the half filled 4f shell of Gd^{3+} and has also practical implications that make $Gd_3N@C_{80}$ a candidate contrast agent for magnetic resonance imaging (MRI) applications [7]. Electron spin resonance experiments on $Gd_3N@C_{80}$ indicate that it can be described as 3 weakly coupled gadolinium ions with a half-filled 4f shell of spin 7/2 [8]. The systematic study on the magnetism of the series $GdnSc_{3-n}N@C_{80}$ $n \in \{1, 2, 3\}$ showed that the magnetisation curve of $n = 1$ fits to a Brillouin function with spin 7/2, while for $n = 2$ and $n = 3$ the data may not be fitted with a Brillouin function, which indicates interaction between different magnetic moments [9]. In the same publication it was also shown by diluting the molecules with non-paramagnetic $Lu_3N@C_{80}$ that the intermolecular interaction is larger than the intramolecular interaction.

Erbium ($4f^{11}$) containing C_{80} fullerenes are investigated also in view of the optical sensitivity of the 4f shell and the possibility of optical switching of the

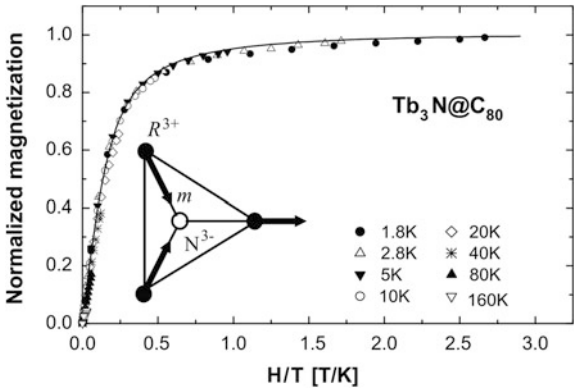

Fig. 11.2 Magnetization M (H/T) of $Tb_3N@C_{80}$ (*symbols*) normalized to saturation. *H* is the external magnetic field μ_0B. The *solid line* is a Brillouin function. *Inset* proposed configuration of the individual rare earth magnetic moments m (*arrows*) in the (R_3N) cluster. From Ref. [12]

magnetization. Between 2 and 300 K the magnetisation of $ErSc_2N@C_{80}$ scales well with the field temperature quotient H/T as it is the case for a Brillouin function, where the J_z levels are degenerate in zero field. It was also shown that for $n = 2$ and $n = 3$ the magnetization does not scale with n [10]. In today's understanding, the poor fit to the parameters expected from the Er $^4I_{15/2}$ Hund ground state suggests the importance of the ligand fields and the n-dependence indicates intramolecular interaction. Though, the anisotropy of the Er 4f shell is not particularly strong, and the N^{3-} ligand field does not promote a high J_z ground state that is favorable for single-molecule magnets.

The case of thulium ($4f^{12}$) showed paramagnetsim that could, for the case of $Tm_3N@C_{80}$, not be saturated in a field of 7 T at 1.8 K [11]. This points to a zero field ground state with low magnetic moment, the details of which still remain to be explored.

The Dresden group focused on ions with large 4f shell anisotropy and a concomitant J_z ground state with large magnetic moment: $Tb_3N@C_{80}$ and $Ho_3N@C_{80}$ [12, 13]. In Fig. 11.2 the magnetic susceptibility of $Tb_3N@C_{80}$ is shown as a function of the H-field/temperature quotient *H/T*. From the apparent paramagnetism a magnetic saturation moment of 18 μ_B per molecule was inferred. This is about a factor of 0.7 smaller than the moment that would be expected from three free Tb^{3+} ions. From these results, noncollinear magnetism was inferred: It was proposed that the ligand field forces the magnetic moments along two possible orientations, parallel or antiparallel to the Tb–N bond. In an external magnetic field, the moments assume the orientation where the projection of the moment is parallel to the external field. These results are important because they indicate that the ground state of Tb_3N and Ho_3N inside C_{80} can be described with a pseudospin model, i.e., with a Hamiltonian where the magnetic interaction is reduced to magnetic moments with two possible orientations. However, at this stage no indications of magnetic interaction between the pseudospins of Tb or Ho were inferred.

11.2 Single-Molecule Magnets

Single-molecule magnets like the famous manganese (Mn_{12}) compound [14] are molecules containing paramagnetic species that maintains their magnetization for milliseconds or longer [15]. In 2004 Ishikawa et al. [16] reported on the discovery of mononuclear lanthanide complexes exhibiting long magnetization relaxation times at high temperatures. This new category of magnets at the single-molecular level was realized with a single Tb^{3+} ion in a phthalocyanine double-decker configuration. For the case of the endofullerenes, it was shown later that the dysprosium-based trimetal nitride endofullerenes, also realize single-ion magnetism, though with much longer spin relaxation times. Furthermore, the use of the trimetal endofullerenes allows to study the interaction between two or three lanthanide 4f ions in an atomically precise environment.

11.2.1 Endohedral Single-Ion Magnets

The metal-nitride-cluster fullerenes (NCFs) encapsulate clusters containing three rare earth ions at the corners of a triangle with a central nitrogen ion, see Fig. 11.1. The rare earth metals adopt a trivalent state, whereas the nitrogen ion and the carbon cage have a closed shell configuration with a formal charge of −3 and −6 respectively. The $R_3N@C_{80}$ molecule is thus diamagnetic unless the endohedral cluster contains lanthanide species with a partially filled 4f shell. The magnetic moment of the system is for this reason solely determined by the spin and orbital momentum of the encapsulated paramagnetic rare earth ions. Still, the surrounding diamagnetic and ionic ligands have a decisive influence on the magnetic properties of the system, as was put forward by Wolf et al. [13]. The concomitant ligand field lifts the degeneracy of the ground state and enables single-molecule magnetism.

Now we consider a LnD_2N cluster containing one paramagnetic lanthanide ion (Ln^{3+}), and diamagnetic species (D^{3+} and N^{3-}). For a free paramagnetic ion, the Hund ground state for the partially filled 4f shell is degenerate in the absence of an external electric or magnetic field. The situation is considerably different for the endohedral cluster where electrostatic interactions with the surrounding ligands, especially the central nitrogen ion, lead to a lifting of the 2J + 1 degeneracy. This means that certain J_z 's become the ground state J_g that is degenerate for $J_g \neq 0$. For the general case the ground state is twofold degenerate $+J_g$, where $+J_g$ has due to time reversal symmetry opposite magnetization to $\pm J_g$. The two states $\pm J_g$ are separated by an energy barrier that limits magnetization reversal by quantum tunneling and thermal excitation. Therefore the ligand field restricts the orientation of the magnetic moment, where the interactions with the N^{3-} ion result in a magnetic anisotropy (easy) axis that must be oriented along the lanthanide–nitrogen bond if the ground state J_g corresponds to the largest possible J_z. Otherwise spin reorientation may occur.

In contrast an isotropic system, where the moment is free to align with an external H field, here the moments orient in the ligand field, and we deal with noncollinear magnetism.

At low temperatures, the ground state doublet determines the magnetic properties of the endohedral lanthanide ion. At zero magnetic field the two components $\pm J_g$ are populated with equal probability, and the system does not exhibit a net magnetization. Applying an external magnetic field lifts the degeneracy of the doublets. The J_g with a parallel component of projected moment along the field direction becomes energetically favorable and by that more populated. The magnetisation adopts an equilibrium value determined by the corresponding Zeeman splitting and temperature of the system. The two components of the ground state doublet are separated by an energy barrier much larger than the Zeeman energy. At low temperatures the thermal energy of the system is not large enough to 'instantaneously' establish equilibrium and kinetics become important. Reaching the equilibrium magnetization is associated with a relaxation time τ, which depends on the temperature and the J_g reversal energy barrier. Consequently, at low temperatures the 4f moment displays a slow response to external magnetic field changes. If the relaxation rate is slow compared to the measurement time, the system exhibits magnetic hysteresis. At small external fields, the hyperfine coupling and the dipole interactions lead to a small splitting of the ground state doublets. Such a lifting of the degeneracy of the ground state doublet allows the magnetization to shortcut the reversal energy barrier and to reverse the magnetization by quantum tunneling of the magnetization (QTM).

11.2.1.1 $DySc_2N@C_{80}$

$DySc_2N@C_{80}$ was the first endohedral metallofullerene where single-molecule magnet behavior was observed, as evidenced by the detection of hysteresis [17]. This discovery was facilitated by the easy accessibility of a circular dichroism beamline. In comparison to the standard tool of superconducting quantum interference device (SQUID) magnetometry, x-ray circular dichroism is sensitive to samples that may be several orders of magnitude smaller than those used for SQUID magnetometry. The drawbacks of the x-ray based methods, as compared to SQUID magnetometry, is price, cryogenic control, and the unavoidable fact that the x-rays and the concomitant secondary electrons demagnetize the molecules [18]. The magnetism of the $DySc_2N@C_{80}$ endofullerene is governed by the spin and orbital momentum of the Dy 4f electrons. X-ray absorption spectroscopy (XAS) provides a tool for probing the magnetism of the system by resonantly exciting 3d $\rightarrow$ 4f transitions, i.e., the $M_{4,5}$ edge. Figure 11.3a displays XAS data recorded from a powder sample of $DySc_2N@C_{80}$ using right (I^+) and left (I^-) polarized x-rays. The polarization dependent absorption is directly related to the unbalance in the spin and orbital momentum of the 4f valence electrons relative to the applied magnetic field and the angular momentum of the x-ray photons. The difference in absorption between the two polarizations provides the x-ray magnetic

circular dichroism (XMCD) spectrum that reflects the spin an orbital magnetic moment of the absorbing Dy ion. By applying a sum rule analysis to the XAS data a powder averaged magnetic moment of the endohedral Dy^{3+} ions of 4.4 μ_B is determined. The extracted value is comparable to that of 4.7 μ_B as obtained with a pseudospin analysis of SQUID data, which indicated a J_z = 15/2 ground state [19, 21, 22]. Figure 11.3b shows an element-specific magnetization curve obtained by recording the maximum XMCD signal at the Dy M_5 edge as a function of the applied magnetic field. The observed hysteresis is a direct indication that the rate at which the magnetization of the single dysprosium ions relaxes to its equilibrium value is slow compared to the measurement time (μ_0dH/dt = 1 T/min). The element specificity of XAS provides the magnetic properties of the individual Dy ions and is related to nonelement sensitive characterization techniques such as SQUID magnetometry. Figure 11.3c displays magnetization curve recorded at 2 K for $DySc_2N@C_{80}$ using SQUID magnetometry. The good agreement with the XMCD data demonstrates that the magnetic moments measured by the SQUID can be attributed to the endohedral dysprosium ions. The deviation between the two data sets is a consequence of x-ray induced demagnetization [18] and temperature calibration.

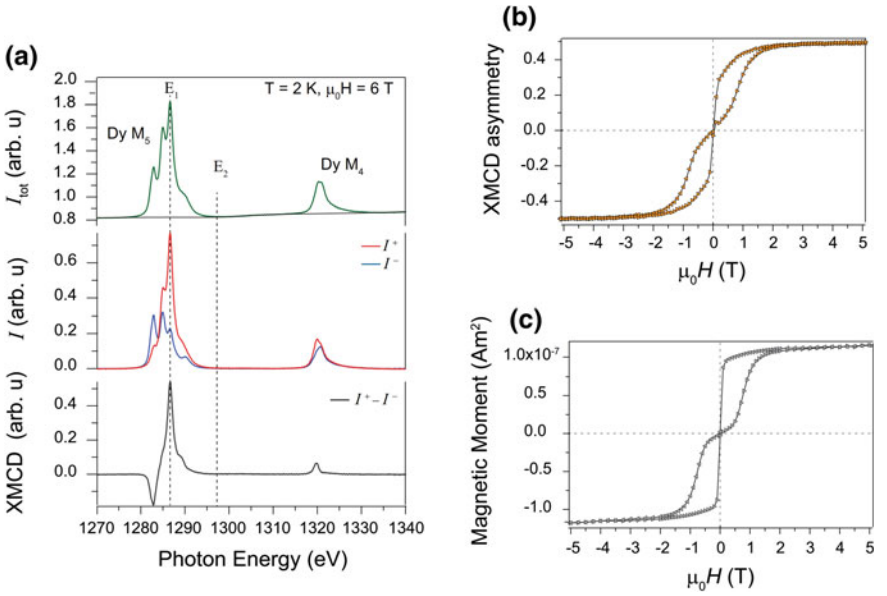

Fig. 11.3 **a** *Top panel* Sum of the x-ray absorption spectra of both x-ray helicities *Itot* recorded at the Dy $M_{4,5}$ edge at 6 T. *Center panel* Polarization dependent x-ray absorption spectra after subtraction of the background, I^+ (*red*) and I^- (*blue*). *Bottom panel* Magnetic circular-dichroism XMCD (I^+–I^-). **b–c** Magnetization curves recorded at 2 K by XMCD (**b**) and SQUID magnetometry (**c**). The element-specific magnetization curve in (**b**) was constructed from the asymmetry $[(I^+_{E_1} - I^+_{E_2}) - (I^-_{E_1} - I^-_{E_2})]/[(I^+_{E_1} - I^+_{E_2}) + (I^-_{E_1} - I^-_{E_2})]$, where E_1 and E_2 are the photon energies in panel (**a**). Adopted from [17]

11.2.1.2 $HoSc_2N@C_{80}$

$HoSc_2N@C_{80}$ also displays single-molecule magnet behavior [20]. Alternating current (ac) susceptibility measurements reveal that this molecule exhibits compared to $DySc_2N@C_{80}$ much faster relaxation of the magnetization. In a small applied magnetic field it was found to be in the order of milliseconds or more than five orders of magnitude faster than for $DySc_2N@C_{80}$. The equilibrium magnetic properties of $HoSc_2N@C_{80}$ indicate as well strong magnetic anisotropy. Figure 11.4 shows the measured magnetization curve of a powder sample, and the corresponding magnetization lifetimes. From the observed magnetization in a powder sample a magnetic moment of 9.15 μ_B was inferred, which is close to a $J_z = 8$ ground state with a LandŽ g factor of 5/4. Both Dy^{3+} and Ho^{3+} have a significant anisotropy in the N^{3-} ligand field and the largest J_z of 15/2 and 8, respectively, assume the ground states, and they have similar thermal demagnetisation barriers [17, 20]. The reason for the large differences in magnetization relaxation times between $HoSc_2N@C_{80}$ and $DySc_2N@C_{80}$ must lie in the nature of the Dy $4f^9$, and the Ho $4f^{10}$ ions, since the two molecules may be considered to be otherwise isostructural. Hyper-fine interaction between the 4f electrons and the nuclear spins may also not explain the strong effect: Dysprosium has four different stable isotopes with different nuclear spins and holmium has one stable isotope with spin 7/2. However, Dy^{3+} ($4f^9$) is a Kramers ion, with an odd number of electrons and a degenerate ground state in zero field and this must be an effective protection by symmetry for the decay of the magnetization via quantum tunneling of the magnetization [20].

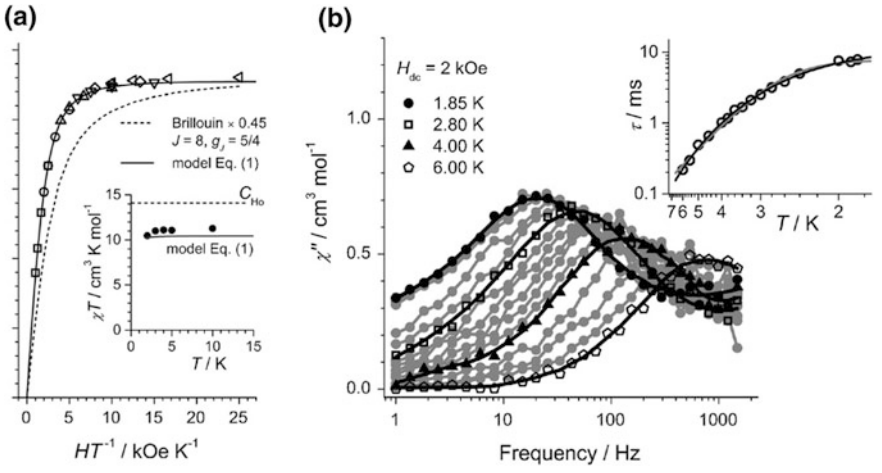

Fig. 11.4 $HoSc_2N@C_{80}$: **a** magnetization curves of $HoSc_2N@C_{80}$ sample. Clearly, the data do not fit a Brillouin function as expected from an isotropic $^5I_8$ Hund ground state of Ho^{3+}. This indicates strong magnetic anisotropy. **b** Alternating current (ac) susceptibility measurements, where the imaginary part χ indicates single-molecule magnetism. The Arrhenius plot in the *inset* indicates for temperatures below 2 K magnetization tunneling times in the order of 8 ms. Adopted from [20]

11.2.2 Polynuclear Endohedral Single-Molecule Magnets

Figure 11.5 displays magnetization curves from the complete dysprosium–scandium endofullerene series $Dy_nSc_{3-n}N@C_{80}$ ($n \in \{1, 2, 3\}$ recorded at 2 K using SQUID magnetometry. As in the case of the single-ion complex $n = 1$, an x-ray absorption characterization was performed for $n = 2$ and $n = 3$ using XMCD to confirm that the detected magnetism of the sample originates from the endohedral Dy ions. The significant difference in the shape of the detected hystereses demonstrates how strongly the endohedral moments interact. Noticeably, there is large remanence for $n = 2$, as compared to a sharp drop in the magnetization at low fields for $n = 1$ and a narrow hysteresis with vanishing zero-field magnetization for $n = 3$. The distinct shape and zero-field behavior is a direct consequence of the magnetic interaction between the endohedral dysprosium ions for $n \in \{2, 3\}$.

The zero-field behavior can be understood by recalling that the n moments of the ground state multiplets are strongly anisotropic and align with the Dy–N ligand field. Under this condition, the magnetic interactions in the ground state are described by a noncollinear Ising model with n pseudospins that can take two orientations, parallel or antiparallel to the corresponding Dy–N axis. The pseudospin picture leads to 2^n magnetic configurations, divided into $2^{(n-1)}$ doublets, where in zero field each doublet consists of two degenerate and time reversal symmetric states with opposite magnetization, see Fig. 11.5b. In the case of $n = 1$,

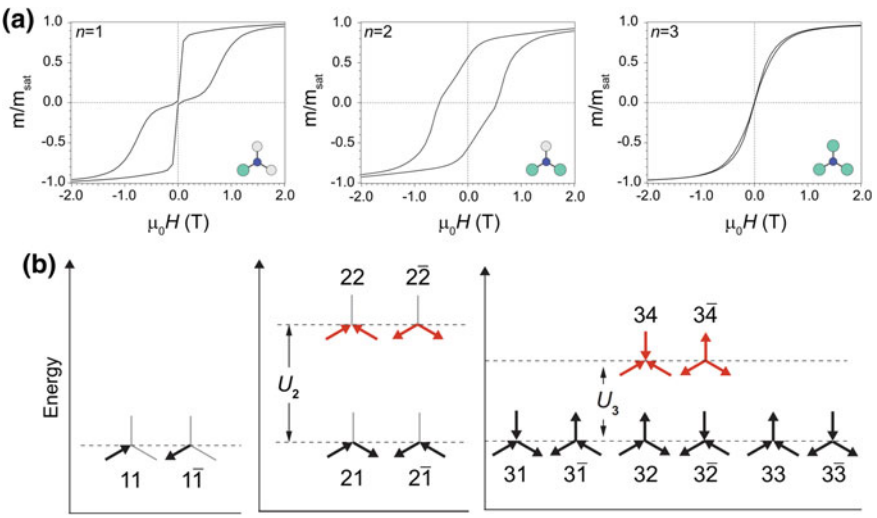

Fig. 11.5 **a** Hysteresis curves for **1–3** recorded using SQUID magnetometry at 2 K with a field sweep rate of 0.8 mTs^{-1}. **b** Ground state magnetic structure for $Dy_nSc_{3-n}N@C_{80}$ based on 2^{n-1} ferromagnetically coupled time reversal symmetric doublets (n, ±d) for $n = 1$–3, where d is the doublet index. The energies U_2 and U_3 are the exchange and dipole barriers for 2 and 3, respectively. Adopted from [19]

no intramolecular interaction occurs. At zero field, the magnetic moment tunnels through the barrier that separates the two states of opposite magnetization. The efficient demagnetization through quantum tunneling of the magnetization (QTM) is clearly seen in the abrupt jump in the magnetization when approaching $\mu_0 H = 0$ T.

11.2.2.1 $Dy_2ScN@C_{80}$

When adding a second Dy ion to the endohedral cluster, the exchange and dipolar coupling of the two moments results in two non-degenerate doublets; a ferromagnetically coupled and an antiferromagnetically coupled one (see Fig. 11.5b).

While the dipolar coupling, which for the given endohedral geometry of an equilateral triangle with 0.36 nm sides and a 10 μ_B moment is in the order of 0.4 meV, is always ferromagnetic, the exchange may be ferromagnetic or antiferromagnetic. The net coupling strength may be extracted from the magnetization curves and turns out to be 1 meV and ferromagnetic [19]. In contrast to the single-ion complex ($n = 1$), no single-tunneling path connects the two time reversal symmetric ground states. This explains the remanence: A magnetization reversal in the di-dysprosium case requires a simultaneous tunneling of the magnetic moments on both dysprosium sites, or crossing of the exchange and dipole barrier of 1 meV that separates the two ground states [19]. Consequently, at low temperatures the system exhibits a blocking of the magnetization that in turn leads to a stabilization of the zero-field magnetization.

As opposed to a ferromagnet, the remanent magnetization in the present case the decay with a time dependent rate τ (see Fig. 11.6a). The nonlinear decay reveals the presence of (at least) two relaxation mechanisms, which has been ascribed to different hyperfine interaction of different Dy isotopes intermolecular [17]. The decay rates for the slower process are displayed in Fig. 11.6b, where a 100 s blocking temperature of about 3.6 K is determined [23]. This 100 s blocking temperature has been determined from the slowest decay constant, and this procedure might not be applicable for other molecules, where extrapolation of the slowest decay channel indicates an initial weight of less than 10% [23]. However, this is among the highest blocking temperatures reported for single-molecule magnets [24–26].

The relaxation times exhibit two temperature regimes, as indicated by the two straight lines. Down to 2 K the relaxation times do not display a temperature independent region, as observed for quantum tunneling of a single moment for $n = 1$. The absence of a quantum tunneling regime is a consequence of the exchange and dipolar coupling of the two moments, where a single- tunneling event is associated with this effective exchange energy. By fitting a sum of two Arrhenius equations to the data, the two energy barriers can be extracted with energies 0.73 and 4.3 meV respectively. The lower barrier ($T < 4$ K) corresponds to the energy gap between the two doublets (Fig. 11.5b). The extracted value of 0.73 meV is in good agreement with the value of 1 meV as determined by a pseudospin analysis of the magnetization curves at 6 K [19]. The second barrier (4.3 meV) is related to

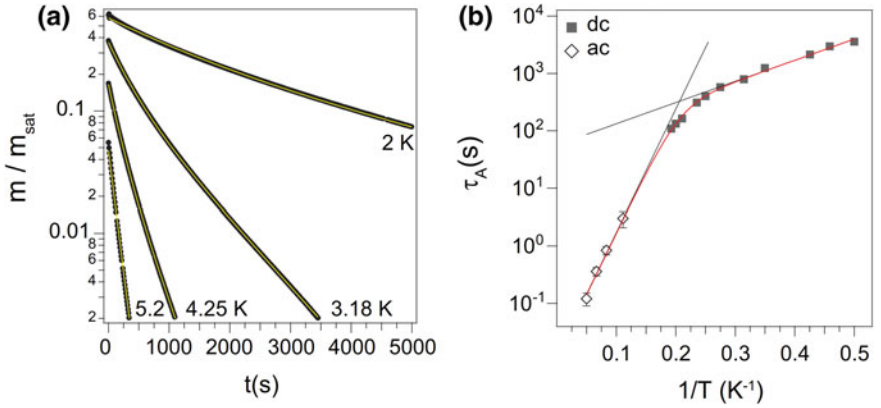

Fig. 11.6 **a** Zero-field relaxation curves for **2** after saturation at $\mu_0 H = 7$ T. *m*sat is the magnetization at 7 T. The *line* corresponds to a fit of a double- ($T < 4.5$ K) and a single- ($T > 4.5$ K) exponential. **b** Corresponding relaxation times for the slower process τA as a function of inverse temperature. *Open symbols* are ac susceptibility results. The *red line* is the best fit of a sum of two Arrhenius equations. Adopted from [19]

relaxation via higher lying excited states. It is worth to be noted that the prefactors of the Arrhenius kinetics are very large compared as to other dysprosium-based SMMs [17, 19].

11.2.2.2 Endohedral SMM's Without Central Nitrogen: $Dy_2TiC@C_{80}$ and $Dy_2TiC_2@C_{80}$

Only recently it was demonstrated that C_{80}-based single-molecule magnets without a central nitrogen ion exist [5]. Figure 11.7 shows magnetic hysteresis for two different isomers of $Dy_2TiC@C_{80}$ and $Dy_2TiC_2@C_{80}$ [5]. The stability of the remnant magnetization can be quantified by determining the temperature at which the zero-field magnetization relaxation time is 100 s, the so-called 100 s blocking temperature (TB100) [23]. For $Dy_2TiC@C_{80}$-I_h T_{B100} is 1.7 K as compared to $T_{B100} = 3.6$ K for $Dy_2ScN@NC_{80}$. The higher T_{B100} value for the nitride cluster-fullerene indicates that the nitride ion in the endohedral cluster is advantageous for longer remanence times. The second isomer $Dy_2TiC@C_{80}$ II has very similar magnetic properties, which indicates that the coordination of the endohedral unit with respect to the cage is of less importance for the magnetism. On the other hand the experimental results assert the central role of the central atom in the endohedral cluster, i.e., nitrogen or carbon. This is further emphasized by the significantly different remanence of $Dy_2TiC_2@C_{80}$ where two carbon atoms share the center.

This new handle for tailoring endohedral fullerenes may not be underestimated, since the isolation of $Dy_2TiC@C_{80}$-I_h is much simpler that that of $Dy_2ScN@C_{80}$-I_h, and it can be expected that the change of the central ionic unit will give new insight on the superexchange mechanism that couples the two Dy ions.

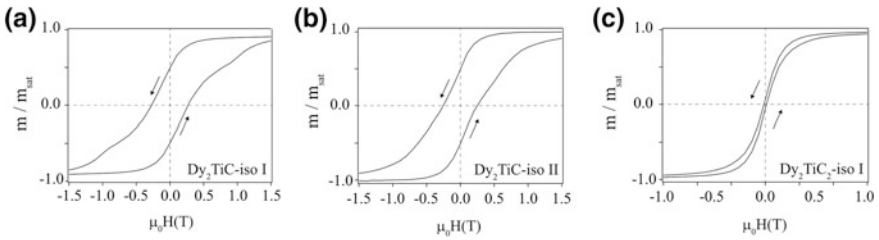

Fig. 11.7 Hysteresis curves for three different TiC-based C_{80} endohedral single-molecule magnets recorded at 1.8 K with a field sweep rate of 5 mT s^{-1}. **a** $Dy_2TiC@C_{80}$ isomer I, **b** $Dy_2TiC@C_{80}$ isomer II **c** $Dy_2TiC_2@C_{80}$, note the different scale of the magnetic field. Adopted from [5]

11.2.2.3 $Dy_3N@C_{80}$

The narrow hysteresis and vanishing zero-field magnetization for $n = 3$ makes it the softest single-molecule magnet of the three. The poor bistability of the three dysprosium moments can be understood by considering a situation where the endohedral ions sit on the corners of an equilateral triangle. The fact that the system exhibits a paramagnetic response to the external field indicates that the three moments are ferromagnetically coupled. For any given pair of ferromagnetically coupled moments, the energy of the system is independent of the orientation of the third, leading to a sixfold degenerate ground state (Fig. 11.5b). This situation is analogous to the textbook case of magnetic (geometric) frustration in an antiferromagnetically coupled isotropic system, where three spins cannot be pairwise antialigned. As in the case of the single-ion complex, there is a single-tunneling path connecting the different ground state configurations, thereby allowing for an efficient demagnetization of the system. Magnetic frustration may thus play a crucial role in the suppression of magnetic blocking in single-molecule magnets.

11.2.3 Endohedral Single-Molecule Magnets on Surfaces

The magnetic bistability and the quantum nature of the molecular spin, make SMMs promising systems for application in spintronics, quantum computing, and high-density storage [27, 28]. A fundamental prerequisite for engineering molecule-based devices is that the magnetic anisotropy and bistability remain unchanged as the molecules are deposited onto substrates or integrated into different device architectures. Creating a stable macrospin in an assembly of nanomagnets will additionally require an ordering of the molecules by, e.g., self-assembly on different surfaces. Deposition of SMMs on reactive surfaces, such as ferromagnetic metals relies on in situ preparation under ultra high vacuum (UHV). In contrast to most SMMs, the endofullerenes discussed in this chapter are particularly stable, survive sublimation and may be easily imaged and manipulated with scanning probes [29–32]. The carbon cage protects the encapsulated magnetic ions from environmental effects.

The structure of $Dy_3N@C_{80}$ on Cu(111) has been studied in great detail by means of scanning tunneling microscopy and resonant x-ray photoelectron diffraction [32]. Figure 11.8 shows a scanning tunneling (STM) image of a monolayer of $Dy_3N@C_{80}$ on Cu(111). While it was not possible to look inside the C_{80} cages with STM, resonant x-ray photoelectron diffraction revealed a preferential orientation of the endohedral clusters parallel to the Cu(111) surface.

As it is shown in the following section, x-ray absorption experiments provide direct insights into the arrangement of the endohedral clusters. The anisotropic charge distribution in the 4f shell allows for the determination of its preferential orientation by comparison of x-ray absorption at different angles, and the corresponding dichroism provides magnetic information. Angle-scanned x-ray absorption spectroscopy (XAS) is thus providing a tool for determining the structural and magnetic anisotropies of highly diluted systems deposited onto surfaces [33]. Figure 11.9a shows the x-ray absorption spectrum from a low coverage of $Dy_2ScN@C_{80}$ on a Rh(111) surface as a function of the angle between the surface normal and the x-ray beam. The density of molecules on the surface is half of a single-molecule thick film (0.5 ML). The angle dependence of the Dy multiplet spectra is a direct fingerprint of an anisotropic 4f orbital charge distribution due to a preferential orientation of the Dy bonds in the system. This effect would not be present for an isotropic distribution of the encaged Dy_2ScN units and, for this reason, indicates an ordering of the endohedral cluster with respect to the surface. The direction of the Dy–N bonds can be determined by comparing the experimental spectra with multiplet calculations performed with the x-ray beam and an external magnetic field applied parallel (I_z), and perpendicular (I_x) to the Dy–N bond. In the present case is the resemblance between the calculated (I_x) spectrum and data measured at normal incidence ($\theta = 0$) in Fig. 11.9b indicates that the endohedral units adopt an orientation parallel to the surface.

Whereas the angle dependence of XAS provides structural information on the system, the corresponding XMCD spectra probe the magnetic anisotropy.

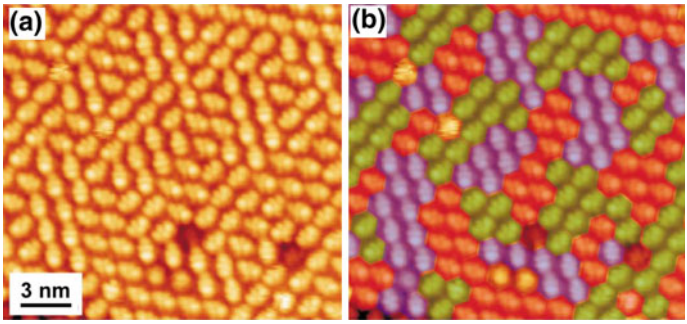

Fig. 11.8 **a** Low temperature scanning tunneling microscopy zoom into a monolayer of $Dy_3N@C_{80}$ on Cu(111). The data show intramolecular orientation and indicate different very small domains (see color coding in the *right panel*). From Ref. [32]

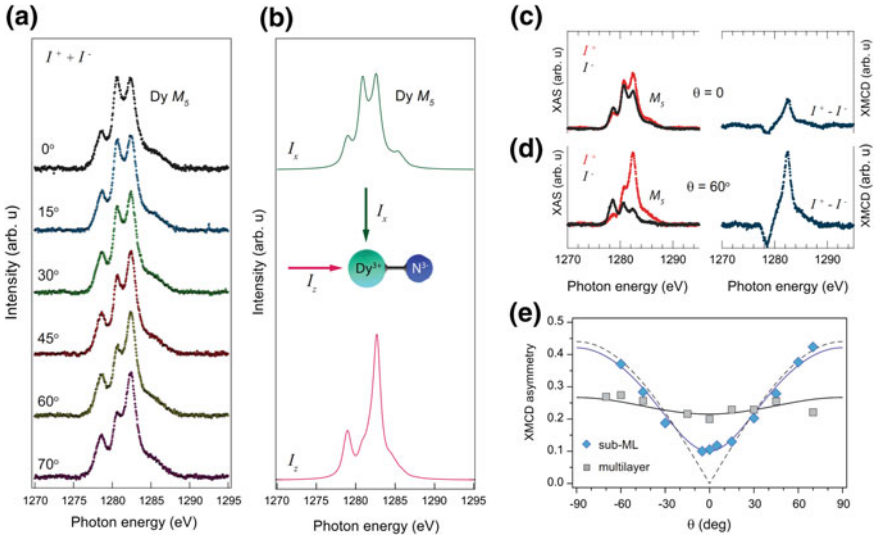

Fig. 11.9 **a** X-ray absorption spectroscopy (XAS) data measured at the Dy M_5 edge from a sub-ML of $Dy_2ScN@C_{80}$/Rh(111) $T \approx 4$ K, $\mu_0 H = 6.5$ T. Each data set is normalized to the integrated intensity. **b** Calculated absorption with the x-ray beam and external field oriented parallel *Iz,* and perpendicular *Ix*, to the magnetic easy axis (Dy–N bond). **c** Polarization dependent XAS spectra (*left panel*), and the corresponding XMCD spectra (*right panel*), measured at an incidence angle of $\theta = 0°$ **c** and $\theta = 60°$ **d**. **e** Angle dependence of the integrated XMCD signal normalized to the integrated XAS over the Dy M_5 edge. The *dashed line* corresponds to the expected angle dependence for magnetic moments oriented parallel to the surface, whereas the *blue line* takes into account a Gaussian distribution, centered in the surface plane and with a standard deviation of 16°. Adopted from [33]

The magnitude of the XMCD signal is determined by the projection of the magnetic moment of the absorbing dysprosium ion onto the direction of the impinging x-rays [33]. For an isotropic system, where the magnetic moments are either randomly distributed or aligned to the external magnetic field, the XMCD signal is independent of the incidence angle. For the sub-ML system, a significant angle dependence is observed (Fig. 11.9c–d) which indicates a macroscopic magnetic anisotropy. The magnetic anisotropy can be further quantified by measuring the XMCD signal for several incidence angles. The angle dependence in Fig. 11.9e demonstrates that the dysprosium moments are indeed predominantly oriented parallel to the surface, with a small out-of-plane fraction inferred by the nonvanishing dichroism at normal incidence. The magnetic ordering is directly related to the strong axial anisotropy of the individual Dy ions and the preferred adsorption geometry of the endohedral cluster imposed by the surface. Also shown in Fig. 11.9e is the corresponding measurement on a system with seven times more molecules (3.5 ML). The weak angular anisotropy is attributed to the residual influence of the surface indicating that the endofullerenes above the first molecular layer do not interact as strongly with the substrate. The multilayer data are thus representative for the bulk phase.

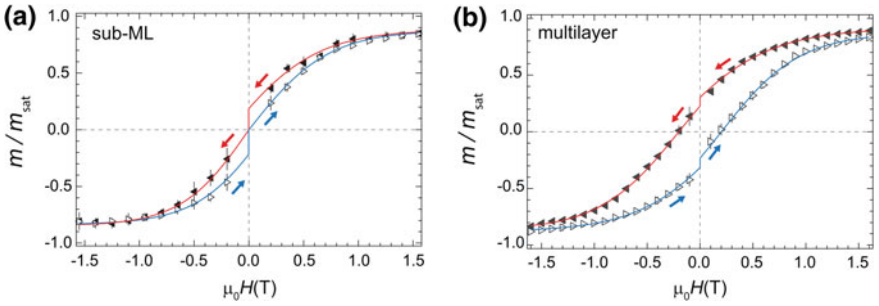

Fig. 11.10 Hysteresis curves measured from a multilayer and a sub-ML of $Dy_2ScN@C_{80}$ on Rh (111) at a magnetic field sweep rate of 2 T/min and a sample temperature of $\sim$4 K. The x-ray flux was 5×10^{10} photons/mm^2/s. The data were recorded with the x-ray beam and the magnetic field at an incidence angle of $\theta = 60°$. The magnetization curves correspond to the average of several independent measurements, where the error bars are the standard deviation at each external magnetic field setting. The *arrows* indicate the ramping direction of the magnetic field, the lines are guides to the eye, and *m*sat is the saturated value at $\pm$6.5 T. The drop in magnetization at zero field is a consequence of the time of 30 s it takes for the magnet to switch polarity. Adopted from [33]

For a fixed temperature and magnetic field sweep rate, the opening of the hysteresis can be taken as a measure of the relaxation times in the system. Comparing the magnetization curves for the two systems thus allows the determination of the influence of the metal substrate. Figure 11.10 shows element specific magnetization curves from the Dy M_5 edge at a field sweep rate of 2 T/min with the x-rays and the magnetic field at an angle of 60° with respect to the surface normal. For bulk samples of $Dy_2ScN@C_{80}$, a significant remanence and coercive field are found (Fig. 11.5a). This is also observed in the multilayer system, where the drop in magnetization at zero field is attributed to the delay of 30 s when changing the polarity of the magnet. From the 25% decrease in magnetization during these 30 s, we derive a remanence relaxation time of 110 s in the multilayer system. Compared to bulk samples measured "in the dark" with SQUID (Fig. 11.6b), this is about four times faster and mainly related to the x-ray induced demagnetization [18].

The much narrower hysteresis for the sub-ML indicates that the magnetic bistability is modified by the proximity of the rhodium surface. From the ratio of the hysteresis openings for the two systems, we obtain a four times faster relaxation rate in the sub-ML and a remanence time under x-ray irradiation at 4 K of about 30 s.

References

1. Kroto HW, Heath JR, O'Brien SC et al (1985) C_{60}—Buckminsterfullerene. Nature 318 (6042):162–163
2. Nakao K, Kurita N, Fujita M (1994) Ab-initio molecular-orbital calculation for C_{70} and seven isomers of C_{80}. Phys Rev B 49(16):11415–11420
3. Stevenson S, Rice G, Glass T et al (1999) Small-bandgap endohedral metallofullerenes in high yield and purity. Nature 401(6748):55–57

4. Svitova AL, Ghiassi K, Schlesier C et al (2014) Endohedral fullerene with μ_3-carbido ligand and titanium-carbon double bond stabilized inside a carbon cage. Nat Commun 5:3568
5. Junghans K, Schlesier C, Kostanyan A et al (2015) Methane as a selectivity booster in the arc-discharge synthesis of endohedral fullerenes: selective synthesis of the single-molecule magnet $Dy_2TiC@C_{80}$ and Its congener $Dy_2TiC_2@C_{80}$. Angew Chem-Int Edit Engl 54(45): 13411–13415
6. Rinehart JD, Long JR (2011) Exploiting single-ion anisotropy in the design of f-element single-molecule magnets. Chem Sci 2(11):2078–2085
7. Shu C, Corwin FD, Zhang J et al (2009) Facile preparation of a new gadofullerene-based magnetic resonance imaging contrast agent with high 1H relaxivity. Bioconjugate Chem 20(6): 1186–1193
8. Náfrádi B, Antal Á, Pásztor Á et al (2012) Molecular and spin dynamics in the paramagnetic endohedral fullerene $Gd_3N@C_{80}$. J Phys Chem Lett 3:3291–3296
9. Svitova AL, Krupskaya Y, Samoylova N et al (2014) Magnetic moments and exchange coupling in nitride clusterfullerenes $Gd_xSc_{3-x}N@C_{80}$ (x = 1-3). Dalton Trans 43:7387–7390
10. Tiwari A, Dantelle G, Porfyrakis K et al (2008) Magnetic properties of $ErSc_2N@C_{80}$, $Er_2ScN@C_{80}$ and $Er_3N@C_{80}$ fullerenes. Chem Phys Lett 466:155–158
11. Zuo T, Olmstead MM, Beavers CM et al (2008) Preparation and structural characterization of the I_h and the D_{5h} isomers of the endohedral fullerenes $Tm_3N@C_{80}$: icosahedral C_{80} cage encapsulation of a trimetallic nitride magnetic cluster with three uncoupled Tm^{3+} Ions. Inorg Chem 47(12):5234–5244
12. Wolf M, Muller KH, Eckert D et al (2005) Magnetic moments in $Ho_3N@C_{80}$ and $Tb_3N@C_{80}$. J Magn Magn Mater 290:290–293
13. Wolf M, Muller KH, Skourski Y et al (2005) Magnetic moments of the endohedral cluster fullerenes $Ho_3N@C_{80}$ and $Tb_3N@C_{80}$: the role of ligand fields. Angew Chem-Int Edit 44(21):3306–3309
14. Sessoli R, Gatteschi D, Caneschi A et al (1993) Magnetic bistability in a metal-ion cluster. Nature 365(6442):141–143
15. Gatteschi D, Sessoli R, Villain J (2006) Molecular nanomagnets. Oxford University Press, New York
16. Ishikawa N, Sugita M, Ishikawa T et al (2003) Lanthanide double-decker complexes functioning as magnets at the single-molecular level. J Am Chem Soc 125:8694–8695
17. Westerström R, Dreiser J, Piamonteze C et al (2012) An endohedral single-molecule magnet with long relaxation times: $DySc_2N@C_{80}$. J Am Chem Soc 134(24):9840–9843
18. Dreiser J, Westerström R, Piamonteze C et al (2014) X-ray induced demagnetization of single-molecule magnets. Appl Phys Lett 105(3):032411
19. Westerström R, Dreiser J, Piamonteze C et al (2014) Tunneling, remanence, and frustration in dysprosium-based endohedral single-molecule magnets. Phys Rev B 89(6):060406
20. Dreiser J, Westerström R, Zhang Y et al (2014) The metallofullerene field-induced single-ion magnet $HoSc_2N@C_{80}$. Chem-Eur J 20(42):13536–13540
21. Vieru V, Ungur L, Chibotaru LF (2013) Key role of frustration in suppression of magnetization blocking in single-molecule magnets. J Phys Chem Lett 4(21):3565–3569
22. Cimpoesu F, Dragoe N, Ramanantoanina H et al (2014) The theoretical account of the ligand field bonding regime and magnetic anisotropy in the $DySc_2N@C_{80}$ single ion magnet endohedral fullerene. Phys Chem Chem Phys 16:11337–11348
23. Westerström R, Popov A, Greber T (2015) An operational definition of the 100 second blocking temperature T_{B100} for single molecule magnets. arXiv:150603657
24. Rinehart JD, Fang M, Evans WJ et al (2011) Strong exchange and magnetic blocking in N_2^{3-}-radical-bridged lanthanide complexes. Nat Chem 3(7):538–542
25. Rinehart JD, Fang M, Evans WJ et al (2011) A N_2^{3-} radical-bridged terbium complex exhibiting magnetic Hysteresis at 14 K. J Am Chem Soc 133(36):14236–14239
26. Le Roy JJ, Ungur L, Korobkov I et al (2014) Coupling strategies to enhance single-molecule magnet properties of erbium-cyclooctatetraenyl complexes. J Am Chem Soc 136(22):8003–8010

27. Leuenberger MN, Loss D (2001) Quantum computing in molecular magnets. Nature 410(6830):789–793
28. Bogani L, Wernsdorfer W (2008) Molecular spintronics using single-molecule magnets. Nat Mater 7(3):179–186
29. Butcher MJ, Nolan JW, Hunt MRC et al (2003) Adsorption and manipulation of endohedral and higher fullerenes on Si(100)-2x1. Phys Rev B 67(12):125413
30. Huang T, Zhao J, Feng M et al (2012) A multi-state single-molecule switch actuated by rotation of an encapsulated cluster within a fullerene cage. Chem Phys Lett 552:1–12
31. Yasutake Y, Shi ZJ, Okazaki T et al (2005) Single molecular orientation switching of an endohedral metallofullerene. Nano Lett 5(6):1057–1060
32. Treier M, Ruffieux P, Fasel R et al (2009) Looking inside an endohedral fullerene: inter- and intramolecular ordering of $Dy_3N@C_{80}$ (I_h) on Cu(111). Phys Rev B 80:081403
33. Westerström R, Uldry A-C, Stania R et al (2015) Surface aligned magnetic moments and hysteresis of an endohedral single-molecule magnet on a metal. Phys Rev Lett 114:087201